12 A Blind Deconvolution Approach for Free-Space Moisture Profile Retrieval at Microwave Frequencies

David Glay, Tuami Lasri

Institut d'Electronique de Microélectronique et de Nanotechnologie,
UMR CNRS 8520 IEMN-DHS, Avenue Poincaré - B.P. 69,
59652 Villeneuve d'Ascq Cedex, France

12.1 Introduction

An outstanding method of sensing moisture is the use of microwaves. Thus, the interaction of microwave radiation with moist substances is of general practical interest in many industrial areas. Consequently, electromagnetic aquametry is a domain that has been intensively studied in recent decades. Many characterization methods have been proposed, enabling large areas (agriculture, chemical, pharmaceutical, and coal industries, civil engineering, etc.) to be studied with this sensing technology [1–5]. Nevertheless, in most cases the test setups were designed to measure the moisture content in the frequency or time domains (reflection and transmission methods, coaxial probes and impedance methods, cavity methods, etc.), for static use in the laboratory. This is the reason why, today, there is a growing interest in proposing systems and methods that can be used outside the laboratories for on-line control. To that end we have developed microwave systems for non-contact moisture sensing applications [6]. These instruments measure the reflection coefficient and/or the transmission coefficient, in magnitude and phase, of a moist material to determine its complex permittivity. Different investigations have been carried out in various fields [7, 8].

This chapter addresses the problem of retrieving the moisture profile of a material presenting a non-uniform moisture distribution. The inhomogeneous dielectric medium, in terms of moisture content, is realized through the construction of a layered material that is made of layers of different moisture content. The configuration proposed permits us to simulate a large range of practical cases. To investigate the possibility of reconstructing, through a one-dimensional model, the moisture profile of the material under test, a free-space technique based on the determination of the reflection coefficient of an antenna is proposed. The collection of the data is performed at 2.45 GHz by using an antenna, fixed at a standoff distance, connected to an S-Parameters Measurement System (SPMS-2450). This apparatus is based on microstrip technology [6].

In the case of inhomogeneous materials characterization, the reflection coefficient is strongly influenced by the radiation pattern of the antenna. One solution to remedy to this problem is to make use of spot focusing antennas. Nevertheless, as far industrial applications are concerned, considerations such as the cost, the fragility, and the dimensions of this sensor have to be taken into account. The solution that has been chosen to overcome these problems is to make use, for example, of a rectangular horn antenna and to develop signal processing tools. Thus, in addition to the physical interacting mechanisms present, signal processing techniques are used to enhance the quality of the one-dimensional reconstructed profile. The proposed method considers that the measured data are the result of a convolution of the true data with a point spread function (PSF) that depends mainly on the operating frequency, the antenna, the characteristics of the structure under test, and the standoff distance between the antenna and the material. Consequently, a modeling effort is undertaken in order to solve the inverse problem by considering a blind deconvolution approach. The chapter describes the moisture profile reconstruction for different material configurations. In particular, subsurface moisture profiles are considered. Simulations and indoor experiments carried out on arrangements of cellular concrete samples are performed to discuss the effectiveness of the method.

12.2 Free-Space Characterization Method

12.2.1 Reflection Coefficient Modeling for a Two-Layer Material

Determination of moisture is very important in many branches of industry. Among the techniques available, microwave moisture measurement procedures are well suited, especially because of the great difference between the dielectric properties of water and most dry materials in the microwave frequency region [9]. Several methods, including transmission, reflection, and resonance techniques, are offered by this characterization means to measure moisture content through indirect methods. In this chapter, the determination is derived by making use of the reflection coefficient of the material under test.

Actually, in many measurement situations in industrial environments, only one side of the material to be characterized is reachable. So, to a great extent, the measurements are based on monostatic methods (one antenna). Another concern when we deal with industrial tests is the necessity to avoid, on the whole, disturbances to the process. To fulfill this requirement a non-contact method is used.

Finally, the measurement system has to be compatible with industrial use in terms of portability, sturdiness, cost, and ease of use. Taking into account all these demands, we propose in Fig. 12.1 a description of the method developed for materials characterization purposes. The material chosen to illustrate the technique is a two-layer material.

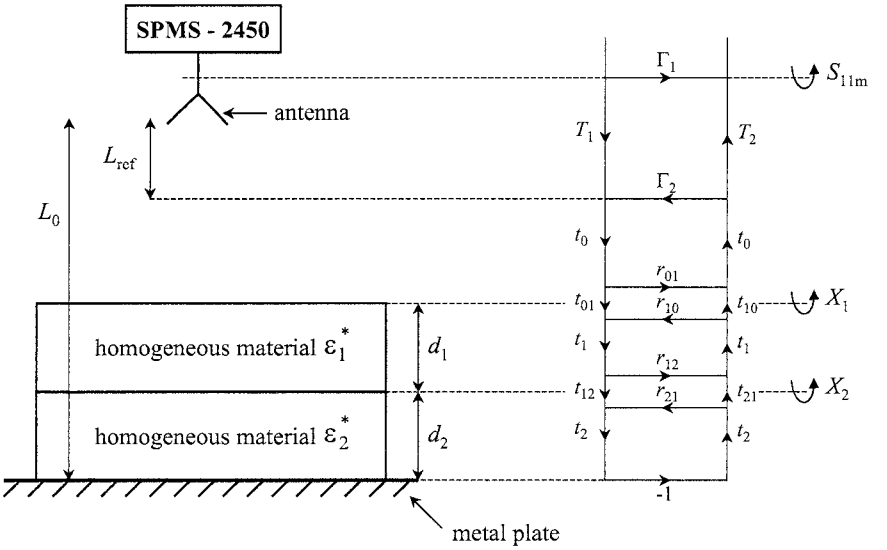

Fig. 12.1. Schematic diagram for a two-layer material characterization

The experimental set-up consists of a system operating at 2.45 GHz (SPMS-2450), realized in the laboratory [6], associated with an antenna (horn antenna) and a metal plate on which the material under test is laid.

The set-up and the measurement configuration chosen permit us to satisfy the expectations mentioned above. Besides the schematic view of the measurement environment we have also given the flow graph that corresponds to the modeling of the propagation phenomena. In this description of the flow graph the following parameters are mentioned:

- Γ_1, Γ_2, and T_1, T_2, which are respectively the reflection and transmission coefficients that take into account the antenna and the space contained between the antenna and the plane located at a distance L_{ref} chosen so that the far-field conditions are fulfilled,
- t_i which represents the transmission coefficient in the medium i (0 for air, 1 for the upper layer, and 2 for the lower one),
- r_{ij} and t_{ij} which define respectively the reflection and transmission coefficients at the interface between media i and j.

The explicit expression of the reflection coefficient S_{11m} calculated from the flow graph is given by

$$S_{11m} = \Gamma_1 + \frac{T_1 T_2 t_0^2 X_1}{1 - t_0^2 \Gamma_2 X_1} \tag{12.1}$$

where

$$X_1 = r_{01} + \frac{t_{01}t_{10}t_1^2 X_2}{1 - t_1^2 r_{10} X_2} \tag{12.2}$$

and

$$X_2 = r_{12} - \frac{t_{12}t_{21}t_2^2}{1 + t_2^2 r_{21}} \,. \tag{12.3}$$

Simulations and measurements are conducted to determine the validity of the reflection coefficient model behavior. To make use of the model (Eq. (12.1)) the parameters Γ_1, Γ_2 and T_1T_2 have to be determined. To that end an experimental procedure which includes the collection of the reflection coefficient for three distances, L_0 and $L_0 \pm \Delta L$, is performed. Thus, the unknown Γ_1, Γ_2 and T_1T_2 are obtained from the resolution of a set of three equations. For this calibration step the material under test is a dry cellular concrete sample ($\varepsilon^*_{\text{dry}} = 2 - 0.1\text{j}$, dry bulk density ρ_{dry} = 0.53 g/cm^3, and thickness $d_1 + d_2$ = 100 mm) whereas the distances L_0, L_{ref}, and ΔL selected are respectively 250 mm, 120 mm, and 20 mm.

Knowing these parameters and the features of the material under test the reflection coefficient $S_{11\text{m}}$ (Eq. (12.1)) can be determined. Comparisons between the model and measured data are made for three materials: air (no material on the plate), a block of dry cellular concrete whose thickness is 100 mm (homogeneous material), and a two-layer material. In this last case the lower layer is a moistened cellular concrete slab (moisture content MC ~ 30%, $\varepsilon^*_{\text{moist}} = 7.0 - 0.8\text{j}$ and thickness d_2 = 50 mm) and the upper layer is a dry cellular concrete slab (d_1 = 50 mm). The moisture content MC is given by

$$MC = \frac{m_{\text{water}}}{m_{\text{dry}}} \,. \tag{12.4}$$

The results obtained are reported in Table 12.1.

Table 12.1. Reflection coefficients obtained from the model and from measurements

Reflection coefficient $S_{11\text{m}}$	Air (no material)	Homogeneous material	Two-layer material
Measurements	–7.0 dB/–0.4°	–11.3 dB/–1.9°	–11.1 dB/–10.1°
Modeling	–7.0 dB/6.0°	–11.3 dB/–1.9°	–10.8 dB/–9.7°

The findings exhibit a fair agreement between the two sets of data and suggest that the model correctly describes the measured reflection coefficient obtained.

In the next section, the composition of the layered material is changed to create a subsurface permittivity profile along the transversal axis (0x).

12.2.2 Construction of a Subsurface Moisture Profile

The previous arrangement (two homogeneous layers) allows us to respond to a particular class of problems in electromagnetic aquametry related to subsurface characterization. In order to expand the range of applications we now treat a slightly different case. The design of the structure proposed is given in Fig. 12.2.

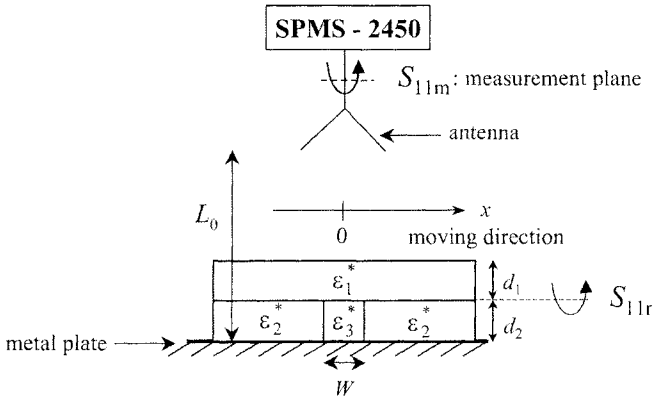

Fig. 12.2. Schematic diagram of the measurement of a subsurface moisture profile

The configuration of interest includes a three-layer material (a layer with a permittivity ε_3^* inserted between two pieces of the same material whose permittivity is denoted ε_2^*) coated with a homogenous material (permittivity ε_1^*). This arrangement allows us to simulate construction of a subsurface moisture profile, or a material presenting a non-uniform moisture content flowing in a pipe, or an unexpected collection of water inside a material, and many others situations. For this particular study we consider a material comprising an area whose moisture content is different from its surroundings ($\varepsilon_1^* \neq \varepsilon_2^* \neq \varepsilon_3^*$).

We propose to demonstrate how we can retrieve, more accurately, information such as permittivity and moisture content derived from the measurement of the one-dimensional reflection coefficient profile (the antenna is displaced above the material under test along the 0x axis at a fixed distance) by using signal processing techniques. In order to test a large range of arrangements we have first performed a simulation study based on the use of commercial software that has proven its wave modeling capabilities for such applications, namely Ansoft High Frequency Structure Simulator (HFSS) [10]. The principal purpose of this investigation was to evaluate the performance and the limitations of the proposed method.

The first test that is presented concerns a cellular concrete sample whose features are a dry permittivity $\varepsilon_{dry}^* = \varepsilon_1^* = \varepsilon_2^* = 2 - 0.1\mathrm{j}$, a dry bulk density $\rho_{dry} = 0.53$ g/cm^3, and a thickness $d_1 + d_2 = 100$ mm, with a moistened area (moisture content $MC \sim 8.5\%$, moist permittivity $\varepsilon_{moist}^* = 3.15 - 0.14\mathrm{j}$, width $W = 70$ mm, and thickness $d_2 = 50$ mm) located at a depth $d_1 = 50$ mm.

This sample is laid on a metal plate situated at a distance $L_0 = 250$ mm from the antenna so that the far-field conditions are fulfilled. The antenna used in the simulation study is an open-ended waveguide. This choice is made only for convenience reasons (simplicity of simulation design and economy of computational time). Prior to the construction of the reflection coefficient profile from the data collected by means of HFSS, we compared the findings obtained by HFSS to those given by the model in three cases. As has been shown in the previous section, knowledge of the parameters Γ_1, Γ_2 and T_1T_2 is needed to use the model. The calculation of these coefficients follows exactly the same scheme. A calibration procedure including the test of a dry sample of cellular concrete, for three different distances ($L_0 = 250$ mm and $\Delta L = \pm 20$ mm), is carried out. The comparisons obtained between the HFSS simulations and the modeling (Eq (12.1)) are reported in Table 12.2.

Table 12.2. Comparison between reflection coefficients obtained from the model and from HFSS simulations

Reflection coefficient S_{11m}	Air (no material)	Homogeneous material	Two-layer material
HFSS simulations	–9.5 dB/–149.7°	–11.6 dB/–123.2°	–10.5 dB/–140.8°
Modeling	–9.1 dB/–144.6°	–11.6 dB/–123.2°	–10.7 dB/–140.0°

This simulation study yields comparable results. Thus, the findings presented in Tables 12.1 and 12.2 indicate that the model predicts the measured and the HFSS data to a good accuracy.

Nevertheless, the data reported in each table are not comparable in themselves because as mentioned above the antenna used in the HFSS simulations is an open-ended waveguide whereas the one selected for the measurement study is a rectangular horn. These two analyses demonstrate that the model behaves in a reasonable way when homogeneous or layered materials are investigated.

However, this description of the propagation phenomena is not sufficient when heterogeneous materials are investigated, especially when the choice of managing without the spot-focusing antenna is taken. The next section is devoted, in particular, to the emphasis of the antenna radiation pattern effects.

12.3 Blind Deconvolution Approach

This part of the chapter is essentially dedicated to HFSS simulations. Actually, as has already been noted, this simulation tool allows us to test a large number of configurations.

12.3.1 Simulation of Reflection Coefficient Profiles

For each configuration two sets of data are collected and organized to construct two different profiles. The first one, called the degraded profile, is established from the data obtained when the antenna is displaced along the material previously defined. The second one, called the true profile, is constructed from the width of the moist area and the reflection coefficient values simulated in the case of a dry material under test (homogeneous material) and in the case of the characterization of a two-layer material (W as large as the dry-part width).

The first example presented concerns the testing of an arrangement that includes a 70 mm wide inclusion. According to the description given above, the true profile is established by using the values in Table 12.2. For more clarity, if we consider, for example, the true magnitude profile, it has been constructed from the magnitudes obtained in the case of testing (Table 12.2) a dry sample (–11.6 dB) and a two-layer material (–10.5 dB).

The resulting profiles for S_{11m} (Fig. 12.2) are shown in Fig. 12.3.

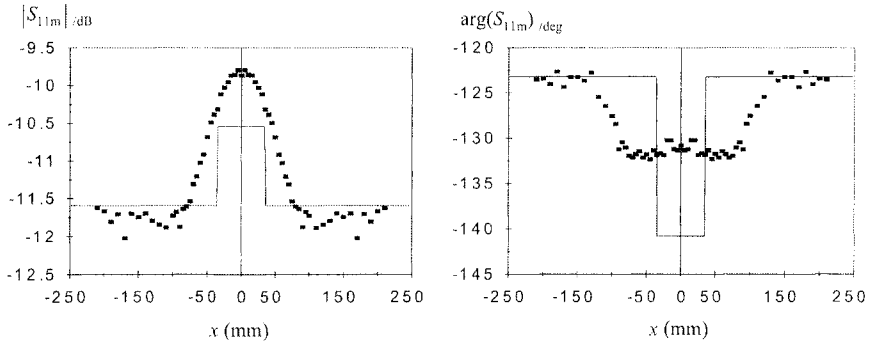

Fig. 12.3. Simulations of $S_{11m}(x)$ for $W = 70$ mm (■: degraded data; ——: true profile)

To take into account the influence of the antenna (matching, free-space propagation, etc.) and the material layer coating the inclusion, we calculate the reflection coefficient S_{11r} in the plane materialized by the dashed line in Fig. 12.2. The results are given in Fig. 12.4.

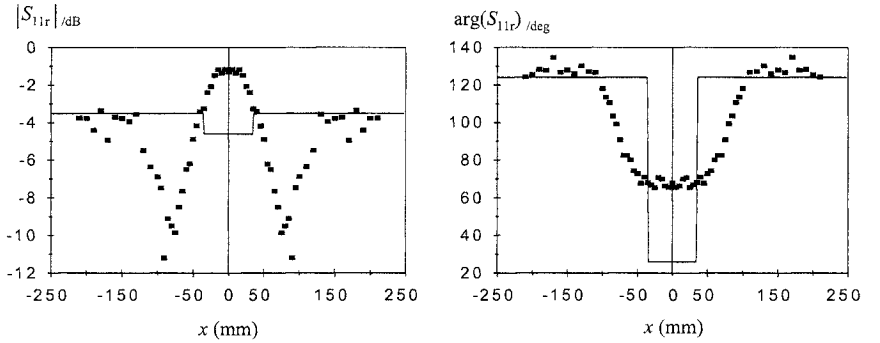

Fig. 12.4. Simulations of $S_{11r}(x)$ for $W = 70$ mm (■: degraded data; ——: true profile)

This figure shows that the magnitude of the reflection coefficient is strongly influenced by diffraction mechanisms. The compensation of such diffraction effects may require specific treatment and represents a limitation of the method. So, we have chosen to work with the phase of the reflection coefficient that clearly shows a convolution relationship between the true and degraded profiles. Thus, the phase degraded profile can be expressed as

$$\arg(S_{11r}\ \text{degraded}) = \arg(S_{11r}\ \text{true}) \otimes h(x) + n(x) \tag{12.5}$$

where $h(x)$ is the PSF, $n(x)$ is additive Gaussian noise, and $\otimes$ is a discrete one-dimensional linear convolution operator.

So, knowing these two profiles (Fig. 12.4), the PSF is calculated from an inversion process of Eq. (12.5).

Before giving the result for this PSF we present simulation data obtained when smaller inclusions are tested. Investigations are performed for three different sizes, $W = 50$ mm, $W = 30$ mm, and $W = 10$ mm. All other parameters of the structure are kept unchanged.

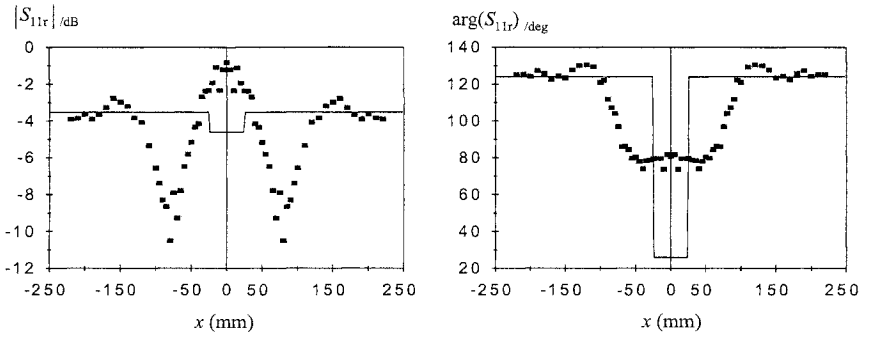

Fig. 12.5. Simulations of $S_{11r}(x)$ for $W = 50$ mm (■: degraded data; ——: true profile)

To simplify the presentation we give only the reflection coefficients $S_{11r}(x)$ deduced from the simulation of $S_{11m}(x)$. We present the simulation results for these three inclusions respectively in Fig. 12.5, 12.6, and 12.7.

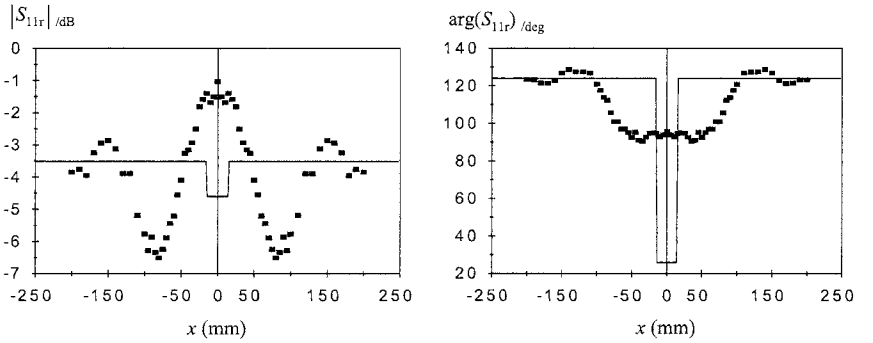

Fig. 12.6. Simulations of $S_{11r}(x)$ for $W = 30$ mm (■: degraded data; ——: true profile)

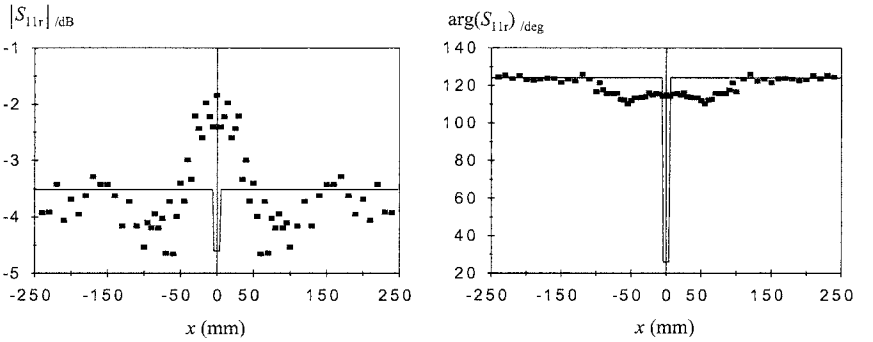

Fig. 12.7. Simulations of $S_{11r}(x)$ for $W = 10$ mm (■: degraded data; ——: true profile)

The simulations performed lead to magnitude and phase shapes relatively similar to those obtained for the case previously treated ($W = 70$ mm). Hence, the conclusions already drawn for the case $W = 70$ mm still stand. It can also be noted that the inclusions are still clearly detected down to $W = 10$ mm, especially if the magnitude is considered. Nevertheless, as we have chosen to take advantage of the reflection coefficient phase (Eq. (12.5)), the restoration of the moisture content is expected to be very difficult for the last configuration tested ($W = 10$ mm). Actually, the phase is not very sensitive to the presence of the smaller inclusion investigated (Fig. 12.7). This case is interesting to appreciate the limitations of the method. In order to illustrate the dependence of the PSF on the material under test, the information given in Figs. 12.4–12.7 is used to determine the PSF for all the configurations ($W = 70$ mm, $W = 50$ mm, $W = 30$ mm, and $W = 10$ mm) studied. The four shapes obtained are presented on the same graph (Fig. 12.8) to observe the degree of similarity.

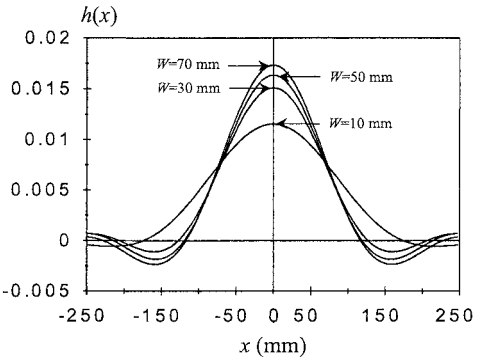

Fig. 12.8. PSF $h(x)$ for different values of W

This comparison shows the sensitivity of the PSF to the arrangement under test. It also demonstrates that the assumption that a PSF calculated in particular situations (frequency, standoff distance, material under test, etc.) remains unchanged is applicable under very restrictive conditions (very low variation of testing conditions). Thus, the first idea that consists in having a calibration procedure to calculate the PSF and assuming it is relatively unvarying in a certain range of experimental conditions is not very satisfactory [11]. So to overcome this difficulty we have made use of a blind deconvolution approach [12–14] for the restitution of the true profiles.

This technique has been successfully used in image processing [15–17] in many scientific and engineering disciplines.

12.3.2 Profile Estimate Results

The problem is that of reconstructing a reliable estimate of the true profile from the received degraded profile. To accomplish this task a blind deconvolution scheme is applied.

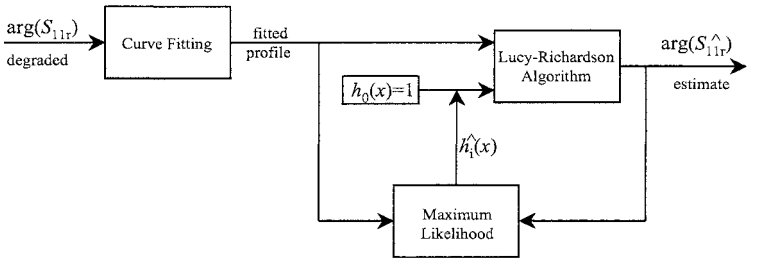

Fig. 12.9. Reconstruction algorithm based on a blind deconvolution approach

Indeed, the blind deconvolution problem is to estimate both the true profile and PSF simultaneously based on the degraded profile and a little a priori information such as non-negativity and support size of the true profile [17]. We give a description in Fig. 12.9 of the blind deconvolution algorithm used.As has been previously mentioned, the parameter of interest is the phase, $\arg(S_{11r})$. As the number of simulation points is not very large (~60 points over a [–200 mm; 200 mm] range) and as they are not regularly spaced (5 mm or 10 mm step), a curve fitting procedure is used to provide more data (512 points) presenting a narrow and regular spacing (2 mm). These functions are the input of an iterative algorithm that needs an initial value of the PSF ($h_0(x) = 1$) to retrieve an estimate of the restored profiles. To illustrate this deconvolution principle, in two examples ($W = 70$ mm and $W = 10$ mm) of a restoration profile we give Fig. 12.10.

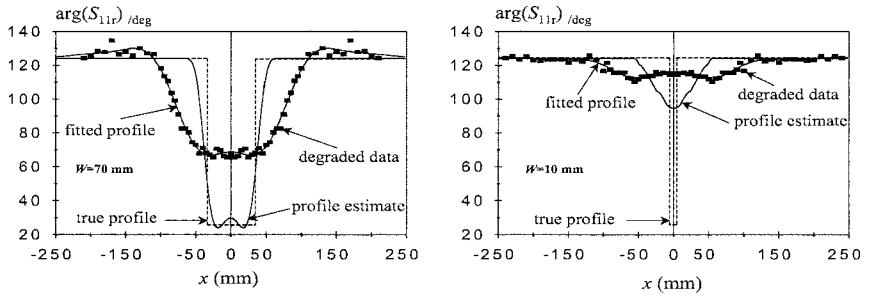

Fig. 12.10. Comparison of reflection coefficient phase profiles for different values of W

The fitted curves in the case of $W = 70$ mm and $W = 10$ mm are obtained respectively by using Eq. (12.6) and Eq. (12.7). The correlation coefficients are respectively equal to 0.996 and 0.968:

$$\arg(S_{11r}\ \text{fitted}) = \left[11.2\cos\left(\frac{x}{19.6}\right) - 66.5\cos\left(\frac{x}{76.8}\right)\right] e^{\frac{-x^2}{14100}} + 124.1 \tag{12.6}$$

$$\arg(S_{11r}\ \text{fitted}) = \left[3.5\cos\left(\frac{x}{19.8}\right) - 11.3\cos\left(\frac{x}{113.2}\right)\right] e^{\frac{-x^2}{22150}} + 124.1\,. \tag{12.7}$$

The results obtained before (fitted profile) and after (profile estimate) the deconvolution process exhibit a great improvement in the restitution of the profile in the case of the configuration including a 70 mm wide inclusion. The profile estimate is reasonably close to the true profile. On the contrary, the situation where an inclusion 10 mm wide is buried at a depth of 50 mm is more complicated. Although the enhancement of the retrieved profile is noticeable, the results are not satisfactory. The profile estimate remains appreciably far from the true profile. Consequently a good prediction of the moisture content from these

results is not conceivable. The usefulness of the treatment of this configuration lies in its illustration of the method's limitation.

We make use of this technique to retrieve a permittivity profile. Among the parameters of practical interest that can be derived from this quantity we find the moisture content. Thus, the next section is devoted to a description of moisture profile restitution. Simulation and experimental studies are tackled to investigate the possibility of using a blind deconvolution approach to enhance the quality of the information retrieved taking into account the assumption made for the magnitude of the reflection coefficient.

12.4 Reconstruction Method of a Moisture Profile

12.4.1 Moisture Profile Simulation

It has already been shown [8] that the permittivity of a moist material ($\varepsilon^*_{\text{moist}}$) can be written as a function of its dry permittivity ($\varepsilon^*_{\text{dry}}$) and bulk density (ρ_{dry}), its moisture content (MC), and the water permittivity ($\varepsilon^*_{\text{water}} = 77 - 12\text{j}$):

$$\sqrt{\varepsilon^*_{\text{moist}}} = \sqrt{\varepsilon^*_{\text{dry}}} + MC\rho_{\text{dry}}\left(\sqrt{\varepsilon^*_{\text{water}}} - 1\right). \tag{12.8}$$

The moist material permittivity is derived from the reflection coefficient: $S_{11\text{r}} = f(\varepsilon^*_{\text{moist}})$ [18]. For the reasons previously presented, the information at our disposal is the profile estimate of the phase. So, we have considered for the magnitude on the $0x$ axis a constant value equal to the one obtained in the case of the dry material testing (Fig. 12.4).

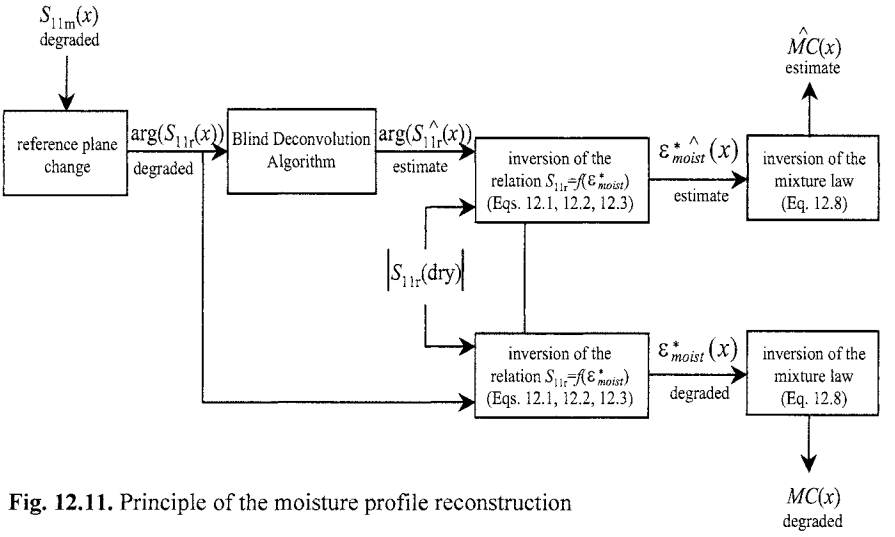

Fig. 12.11. Principle of the moisture profile reconstruction

The difficulty in retrieving the magnitude profile is one of the limitations of the method. Nevertheless, as the contrast permittivity investigated in this simulation is not very important, this approximation does not induce too hard a penalty.

The moisture profile reconstruction principle is detailed in Fig. 12.11 where all the stages of the method are given.

This technique is applied to the sample whose moist inclusion width is $W = 70$ mm. The different reflection coefficients (S_{11m}, S_{11r}, $S_{\hat{11}r}$) appearing in the flowchart of this reconstruction algorithm have been presented, for $W = 70$ mm, in Figs. 12.3, 12.4, and 12.10. The permittivity profile is computed from these data according to the diagram given in Fig. 12.11.

Fig. 12.12 shows a comparison of the different complex permittivity profiles calculated. These results indicate that the profile of the real part of the complex permittivity is retrieved to an acceptable accuracy whereas the imaginary part is not restored in a good manner. This is not surprising considering the assumption made for the magnitude of the reflection coefficient ($|S_{11r}(x)| = |S_{11r}(\text{dry})|$).

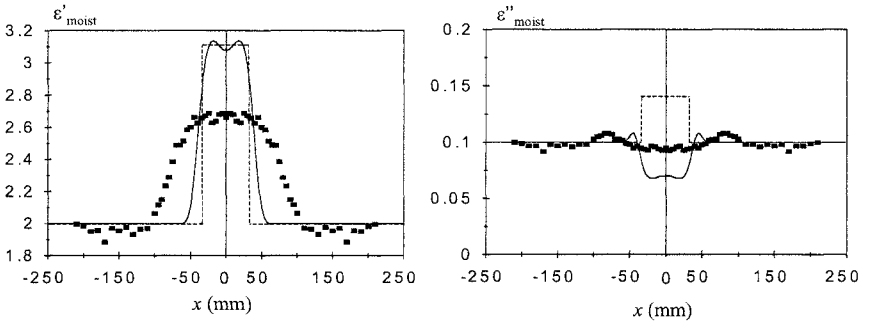

Fig. 12.12. Comparison of the complex permittivity profiles for $W = 70$ mm (■: degraded data; ----: true profile; ——: profile estimate)

Once again, these results ($\varepsilon''_{\text{moist}}$) are not given for their relevance but only to indicate the degree of validity of the method.

According to the description given in Fig. 12.11, we calculate the moisture content profiles from the data given in Fig. 12.12 and the Eq. (12.8).

A comparison of the different moisture profiles calculated, for the four configurations investigated, is presented in Fig. 12.13.

For $W = 70$ mm and $W = 50$ mm the findings show that the moisture content profile is comparable to the true profile. The data observed after the deconvolution process enhance the quality of the retrieved profile. When the antenna is just over the inclusion ($x = 0$) the degraded data (before deconvolution) indicate a moisture content of about 5.5% for $W = 70$ mm and 4.5% for $W = 50$ mm instead of 8.5%, whereas the value retrieved after the deconvolution treatment is correct. For $W = 30$ mm the shape is globally well restored; however, there are resolution problems, related to the diminution of the signal to noise ratio.

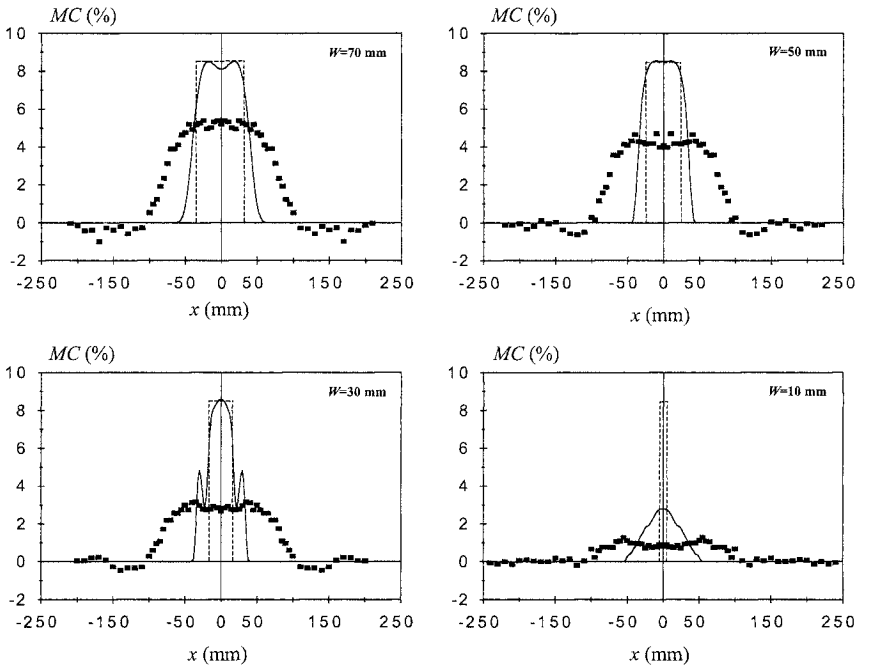

Fig. 12.13. Comparison between moisture profiles for different values of W (■: degraded data; ----: true profile; —— : profile estimate)

But, once again, it can be noticed that for the position $x = 0$ the deconvolution process leads to a very good estimate moisture content. An examination of the last case, $W = 10$ mm, shows that the model is not valid for this size of inclusion and this level of moisture content. Thus, except for the last configuration, the different simulations performed clearly show that the method is very efficient when subsurface detection of a zone presenting a moisture content different from its surroundings is required. In addition, the moisture content of this zone is well estimated. Concerning the reconstruction of a moisture profile, it has been shown that the technique based on a blind deconvolution approach brings a noticeable improvement in the retrieved profile quality, at least for a moist inclusion with a width greater than 10 mm. After this theoretical analysis based on simulation results we propose to perform indoor experiments to analyze the performance of the method on real data.

12.4.2 Moisture Profile Measurement

The measurement study is performed by considering the same material investigated in the simulation analysis. Actually, the structure under test is made of four blocks of cellular concrete. Three of them are dry and the fourth is moist. The arrangement is realized according to Fig. 12.2. Taking into consideration the

simulation results, we have chosen an inclusion whose thickness d_2 and width W are equal to 50 mm, buried at a depth d_1 equal to 50 mm. For the moisture content of this slab we have decided to increase the difficulty by considering a lower moisture level compared to the simulation tests. Therefore the moisture content presented by the inclusion is $MC = 4\%$.

The method used to reconstruct the moisture profile is copied from the development described in the simulation analysis. The first step consists in measuring the reflection coefficient S_{11m} of the structure under test. The results of this characterization are given in Fig. 12.14.

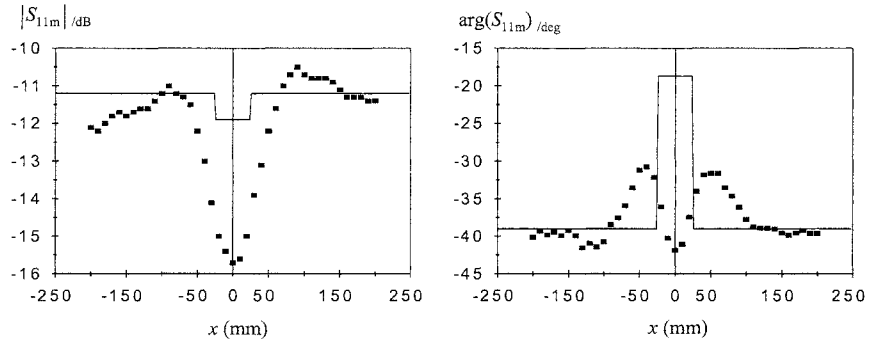

Fig. 12.14. Measurement of reflection coefficient profile $S_{11m}(x)$ for $W = 50$ mm (■: measured data; ——: true profile)

As for the previous simulation data we have also presented in this graph the true profile that should be obtained. This one is constructed from knowledge of the inclusion width and the true moisture content (MC = 4%) that gives the true complex permittivity of the moist material ($\varepsilon^*_{moist} = 2.49 - 0.16j$) by using Eq. (12.7) and finally the true reflection coefficient S_{11m} (Eqs. (12.1–3)).

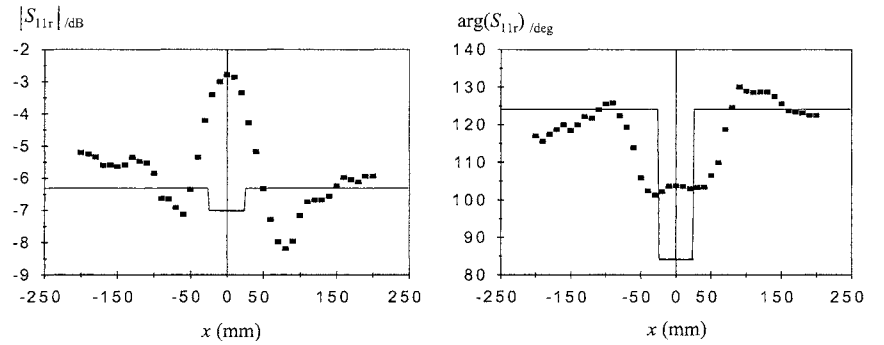

Fig. 12.15. Calculation of the reflection coefficient profile $S_{11r}(x)$ for $W = 50$ mm (■: measured data; ——: true profile)

The data collected for S_{11m} are the basis for the calculation of the reflection coefficient in the plane located at the interface between the upper block and the three others (Fig. 12.2). The findings for this parameter, S_{11r}, are presented in Fig. 12.15.

The results exhibit a shape that is not symmetrical. This is essentially due to a slight slope along the $0x$ axis and probably to a difference between the state of the blocks on each side of the moist slab. Actually, after verification it was shown that the block on the left ($x < 0$) was not entirely dry. A few tenths of a percent were present in certain zones of the sample. This residual moisture is the result of the drying of this sample that was initially moistened for other tests. Taking into account these experimental difficulties, we have obtained symmetry by considering only the data collected for positive values of x.

As already described in the simulation study, a curve fitting procedure is used (Eq. (12.9)). The correlation coefficient is equal to 0.994:

$$\arg(S_{11r}\ \text{fitted}) = \left[99.4\cos\left(\frac{x}{26.8}\right) - 118.9\cos\left(\frac{x}{31.5}\right)\right] e^{\frac{-x^2}{5520}} + 124.1\,. \tag{12.9}$$

The profile estimate is then recovered by applying the algorithm based on blind deconvolution given in Fig. 12.9. Fig. 12.16 shows all the profiles (fitted, estimated, and true) to make a comparison.

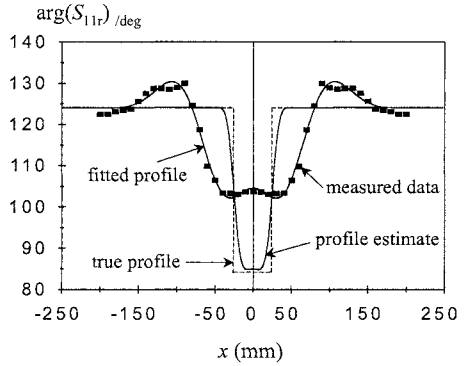

Fig. 12.16. Comparison of reflection coefficient phase profiles for $W = 50$ mm

The results show a sensitive enhancement of the retrieved profile.

According to the description given in Fig. 12.11 for the moisture profile reconstruction we calculate the permittivity profile. The comparison between the estimated and true profiles is shown in Fig. 12.17.

We can conclude that there is good agreement between the two kinds of data in the case of $\varepsilon'_{moist}(x)$. On the contrary the $\varepsilon''_{moist}(x)$ profile is not restored in a good manner. Bearing in mind the level of moisture investigated, this result was, however, expected (low-loss material).

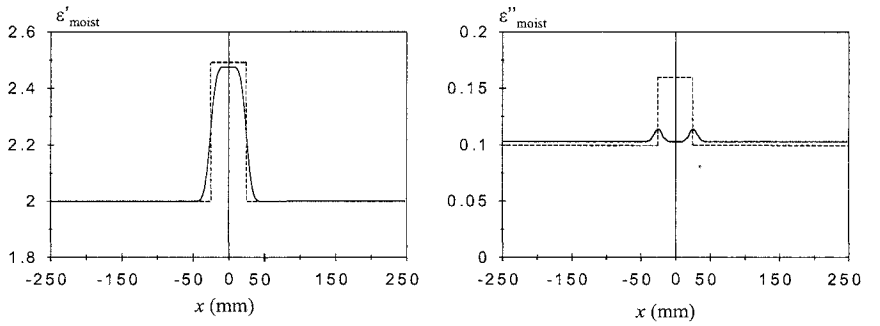

Fig. 12.17. Profiles comparison of the complex permittivity for $W = 50$ mm (----: true profile; ——: profile estimate)

Finally, to complete the process we give in Fig. 12.18 a comparison of the different moisture content profiles.

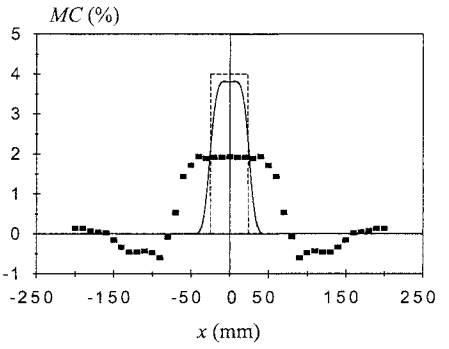

Fig. 12.18. Comparison of moisture content profiles for $W = 50$ mm (■: measured data; ----: true profile; ——: profile estimate)

These results demonstrate the importance and the benefits of using signal processing tools to enhance the quality of a recovered profile. The method proposed seems to be promising, especially because the moisture content investigated is very low.

12.5 Conclusion

The use of microwave techniques has been investigated for many applications during the last few decades. The measurement of moisture content is one field where this technology has found a very large and successful development.

Nevertheless, for a long time many applications were based only on microwave capabilities. The performance of the characterization method was mainly related to the accuracy of determining the parameters measured by the microwave system (for example, magnitude and phase of the reflection coefficient or transmission coefficient) that lead to the quantity of interest such as moisture content. Today, we can show that with adequate signal processing treatment we are able to improve the quality of the information retrieved. The sensing problem has to be considered in terms of sensitivity with respect to the quantity of interest and also with aspects related to the development of signal processing tools, while maintaining acceptable costs. In this particular study the objective was to investigate the possibility of reconstructing a subsurface moisture profile for the purpose of detecting, locating, and qualifying a zone presenting a moisture content different to its surroundings. Simulation data have shown that the technique is relevant for a relatively small inclusion with regard to the wavelength. Confirmation of the good behavior of the proposed model has been obtained through indoor experiments. It can also be noted that these encouraging results have been obtained for inclusions presenting a low moisture content. In the simulation and experimental investigations the buried depth of interest was chosen equal to 50 mm, but the method is still applicable for greater burial distances.

References

1. Kraszewski AW, Trabelsi S, Nelson SO (2001) Broadband free-space microwave wheat permittivity measurements. In: Kupfer K (ed) Fourth international conference on electromagnetic wave interaction with water and moist substances, Weimar, pp 195–202
2. Kupfer K (2001) Material properties – measuring methods – applications. In: Kupfer K (ed) Fourth international conference on electromagnetic wave interaction with water and moist substances, Weimar, pp 517–527
3. Fischer M, Nyfors E, Vainikainen P (1996) On the permittivity of wood and the on-line measurement of veneer sheet. In: Kraszewski A (ed) Microwave aquametry - electromagnetic wave interaction with water-containing materials, IEEE Press, Piscataway, NJ, pp 347–354
4. Kent M, Knöckel R, Daschner F, Berger UK (1999) Measurement of composition and prior treatment of foodstuffs using complex dielectric spectra. In: Third workshop on electromagnetic wave interaction with water and moist substances, Athens, GA, pp 20–24
5. Zhang Y, Okamura S (2001) New function of dielectric properties for density-independent moisture measurement. In: Kupfer K (ed) Fourth international conference on electromagnetic wave interaction with water and moist substances, Weimar, pp 111–116
6. Lasri T, Glay D, Mamouni A, Leroy Y (2000) Development of microwave moisture measurement system around microstrip complex correlator. Sensors update, vol 7, Wiley-VCH, Weinheim, pp 233–248
7. Lasri T, Glay D, Mamouni A, Leroy Y (1996) A low cost microwave system for non destructive control of textile webs. J Microwave Power Electromag Energy 31(2):122–126

8. Lasri T, Glay D, Mamouni A, Leroy Y (1999) Free-space moisture measurements of cellular concrete. In: Third workshop on electromagnetic wave interaction with water and moist substances, Athens, GA, pp 184–188
9. Kraszewski A (1991) Microwave aquametry - needs and perspectives. IEEE Trans Microwave Theory Tech 39(5):828–835
10. Glay D, Lasri T, Mamouni A, Leroy Y (2000) A 35 GHz vector system for non destructive applications. In: Thompson DO and Chimenti DE (eds) Review of progress in quantitative non destructive evaluations, vol 19A. American Institute of Physics, New York, pp 579–586
11. Glay D, Lasri T, Mamouni A (2001) Non destructive permittivity profile retrieval of non-planar objects by free-space microwave techniques. Subsurf Sensing Technol Appl 2(4):391–409
12. Ayers GR, Dainty JC (1988) Iterative blind deconvolution method and its applications. Opt Lett 13(7):547–549
13. Miura N, Baba N (1992) Extended-object reconstruction with sequential use of the iterative blind deconvolution method. Opt Commun 89:375–379
14. Tsumuraya F, Miura N, Baba N (1994) Iterative blind deconvolution method using Lucy's algorithm. Astron Astrophys 282(2):699–708
15. Djafari AM, Qaddoumi N, Zoughi R (1999) A blind deconvolution approach for resolution enhancement of near-field microwave images. SPIE Proc 3816: 274–281
16. Jalobeanu A, Blanc-Féraud L, Zerubia J (2000) Study of the estimation of instrumental parameters in satellite imaging. INRIA Research Report RR-3957
17. Kundur D, Hatzinakos D (1998) Recursive blind deconvolution of still images based on nonnegativity and support constraints. IEEE Trans Signal Process 46(2):375–3
18. Glay D, Lasri T, Mamouni A, Leroy Y (2001) Free-space moisture profile measurement. In: Kupfer K (ed) Fourth international conference on electromagnetic wave interaction with water and moist substances, Weimar, pp 235–242